

In Vivo Intracardiac Vector Flow Imaging Using Phased Array Transducers for Pediatric Cardiology

Solveig Fadnes, Morten Smedsrud Wigen, Siri Ann Nyrnes, and Lasse Lovstakken

Abstract—Two-dimensional blood speckle tracking (ST) has shown promise for measuring complex flow patterns in neonatal hearts using linear arrays and high-frame-rate plane wave imaging. For general pediatric applications, however, the need for phased array probes emerges due to the limited intercostal acoustic window available. In this paper, a clinically approved real-time duplex imaging setup with phased array probes was used to investigate the potential of blood ST for the 2-D vector flow imaging of children with congenital heart disease. To investigate transmit beam pattern and tracking accuracy, straight tubes with parabolic flow were simulated at three depths (4.5, 7, and 9.5 cm). Due to the small aperture available, diffraction effects could be observed when approaching 10 cm, which limited the number of parallel receive beams that could be utilized. Moving to (slightly) diverging beams was shown to solve this issue at the expense of a loss in signal-to-noise ratio. To achieve consistent estimates, a forward-backward tracking scheme was introduced to avoid measurement bias occurring due to tracking kernel averaging artifacts at flow domain boundaries. Promising results were observed for depths <10 cm in two pediatric patients, where complex cardiac flow patterns could be estimated and visualized. As a loss in penetration compared with color flow imaging is expected, a larger clinical study is needed to establish the clinical feasibility of this approach.

Index Terms—Ultrasound blood flow imaging, speckle tracking, vector flow imaging, pediatric cardiology.

I. INTRODUCTION

IN PEDIATRIC cardiology, ultrasound Doppler imaging is a highly useful tool for detecting abnormal blood flow patterns related to pathology. Abnormalities or diseases of the heart have a prevalence of 8 out of 1000 live births [1]. Intracardiac flow in pediatric patients with congenital heart disease can be complex due to septal defects, valvular abnormalities, arterial or venous anomalies, and hypoplastic, hypertrophic or dilated cardiac chambers. Furthermore, surgical treatment may lead to changes in flow that is not fully mapped or understood, and, which may be related to both short and long term outcomes.

Color flow imaging (CFI) is the conventional method to measure blood flow velocity patterns in a 2-D or 3-D region, where velocities are color-coded and visualized together with the B-mode image. For blood velocity quantification, spectral

Doppler methods are commonly used, where the full spectrum of blood velocities from a specific point or line in the ultrasound image is displayed. However, these Doppler-based methods only measure the blood velocity component along the ultrasound beam axis and cannot capture the 3-D nature of the blood flow. Interpretation of the color flow images is thus required to comprehend the true flow patterns, which is challenging for complex (secondary) flow patterns. These limitations may lead to missed or false diagnoses [2], [3]. Methods for improved blood velocity estimation, quantification, and visualization in 2-D or 3-D would decrease the need of interpretation when evaluating the cardiac anatomy and function, and could potentially introduce new clinical markers for diagnosis and follow-up [4].

One approach to obtain the 2-D or 3-D vector flow information is to utilize blood speckle tracking (ST), where the movement of the blood speckle is tracked from frame to frame, providing an estimate of the blood velocity vector [5]. When combined with the high-frame-rate imaging techniques such as plane wave imaging, it was shown in [6] that angle-independent cardiac blood velocity information could be achieved using a linear array probe. Using a linear array probe for cardiac applications is first of all feasible when imaging newborns. However, the pediatric patient group includes a broad spectrum of patients from the smallest premature baby up to adult size. Thus, for pediatric cardiology in general, phased array probes are today the preferred standard probes to image through the intercostal space. Feasibility for 2-D vector velocity maps from phased array imaging has previously been shown for simulations and the experimental setup of a newborn heart model [7], and *in vivo* in adults [8]. In both cases, noncompounded diverging beams and blood ST were used.

While imaging using broad transmit and parallel receive beams can benefit from a much higher frame rate than conventional focused imaging, the loss in signal-to-noise ratio (SNR) and penetration depth can be a limiting factor, leading to a tradeoff with frame rate. Sufficient removal of the strong tissue echo is also more challenging, due to the increased sidelobe and clutter level, compared with focused imaging. Furthermore, the small aperture of phased array probes may influence the accuracy of the ST velocity estimates, due to diffraction focusing effects and the depth-dependent image resolution. To increase SNR and improve blood velocity estimation, contrast agents can be injected into the patient's bloodstream and tracked as in echo-particle image velocimetry (echo-PIV) [4], [9], [10]. Contrast agents are, however, neither desired in a daily routine examination nor currently approved in pediatric cardiology.

Manuscript received December 23, 2016; accepted March 25, 2017. Date of publication April 24, 2017; date of current version August 28, 2017. (Corresponding author: Solveig Fadnes.)

S. Fadnes, M. S. Wigen, and L. Lovstakken are with the Department of Circulation and Medical Imaging, Norwegian University of Science and Technology, 7491 Trondheim, Norway (e-mail: solveig.fadnes@ntnu.no).

S. A. Nyrnes is with the Department of Pediatrics, St. Olav's University Hospital, 7030 Trondheim, Norway, and also with the Department of Circulation and Medical Imaging, Norwegian University of Science and Technology, 7491 Trondheim, Norway.

Digital Object Identifier 10.1109/TUFFC.2017.2689799

Our aim of this paper was to develop and investigate the blood ST methods based on phased array imaging for pediatric cardiology without the use of contrast agents. A clinically approved imaging setup was implemented for phased array probes, utilizing broad pulses to acquire real-time color flow data at high-data acquisition rates, as also described in [11]. Two pediatric patients (one newborn and one 11 years old) were included in the study. To investigate the possible penetration depths with our clinically approved setup, the pressure fields for unfocused, deeply focused, and defocused (diverging) waves were measured in a water-tank setup. In addition, the accuracy of the velocity estimator as a function of depth and steering angles was also investigated in simulated straight tubes with parabolic flow.

II. METHODS

A. *In Vivo* Acquisition

A real-time duplex imaging setup based on broad transmit pulses was set up on a GE Vivid E9 scanner with a dedicated research software (GE Vingmed, Horten, Norway). For the color flow acquisition, the transmit pulses were deeply focused (30 cm) to insonify a broad sector for each transmit, and a multiline acquisition (MLA) with 16 parallel receive beams was used. This both increases overall frame rate, and also enables ST on a large coherent region acquired at the Doppler pulse repetition frequency (PRF). Fully plane (unfocused) or diverging (negative focus) transmissions were not available for clinical testing. The acquisition was clinically approved for the GE 9L linear array probe and two-phased array pediatric probes (GE 6S and 12S). With 16 parallel receive lines per transmit beam, several (3–9) transmissions were needed to get the desired region of interest (ROI). For the B-mode images, conventional focused transmit beams were used to obtain sufficient image quality. The resulting duplex frame rate was 40–80 frames/s, depending on the Doppler packet size (8–22), image depth (<10 cm), and ROI width.

IQ data from the color flow acquisition were stored after real-time beamforming on the scanner. The data were further processed offline to generate vector velocity maps of the blood flow, as described in Section II-E. The imaging sequences were clinically approved before the study started and were within the guidelines from the U.S. Food and Drug Administration. The image acquisition parameters for the *in vivo* recordings are listed in Table I.

Two patients were imaged using both the 9L linear array and the 6S phased array probe. Patient 1 was born with a pulmonary valve (PV) stenosis and was 10 days old and weighed 3080 g at the time of the ultrasound recordings. Patient 2 was 11 years old (35.6 kg and 149.8 cm tall) at the time of the recordings. This patient had a dilated cardiomyopathy (DCM) of unknown cause and an ejection fraction of only 20%. Written informed consents were obtained from the parents of the children before examination and the study was approved by the Norwegian Regional Committee for Medical and Health Research Ethics.

B. Straight Tube Simulations

To investigate the accuracy of the velocity estimator using the clinically approved *in vivo* setup, Field II [12], [13] was

TABLE I
In Vivo ACQUISITION PARAMETERS

Patient 1 (PV stenosis)	9L	6S
Pulse center frequency [MHz]	5	4.5
PRF [kHz]	10	9
Packet size	16	22
V_{Nyquist} [m/s]	0.82	0.77
No. of tx beams	7	5
Tracking kernel size [mm ²]	1x1	
Spatial Gaussian smoothing [mm ²]	5x5	
Temporal smoothing [ms]	40	
Patient 2 (DCM)	9L	6S
Pulse center frequency [MHz]	4.5	3.7
PRF [kHz]	6	5
Packet size	8	16
V_{Nyquist} [m/s]	0.51	0.53
No. of tx beams	12	8
Tracking kernel size [mm ²]	1.5x1.5	
Spatial Gaussian smoothing [mm ²]	7x7	
Temporal smoothing [ms]	40	

used to simulate a parabolic straight tube flow for an imaging sequence with seven deeply focused (30 cm) transmit pulses covering an opening angle of 60°, using a similar pediatric phased array probe. The pulse center frequency was 3.3 MHz, the PRF was 3 kHz, and the Doppler packet size was 16. The straight tubes were horizontally placed at three depths (4.5, 7, and 9.5 cm) and had a constant parabolic flow with a maximum velocity of 1 m/s. To evaluate the expected mean and standard deviation of the velocity estimator, 20 realizations of the Doppler frame were simulated. Both accuracy as a function of depth and steering angle were investigated. The simulation parameters are listed in Table II.

While the deeply focused setup was used due to approved safety measurements, it could be beneficial with deeper or slightly diverging beams to maintain a wide and more uniform beam at deeper distances. The straight tube simulations were further used to simulate speckle patterns under the different acquisition schemes, followed by a ST performance comparison.

C. Beam Profile Measurements

The Onda AIMS III scanning system (Onda Corporation, USA) was used with the Onda HMB-0200 membrane hydrophone to measure pressure fields for the GE 6S probe. The clinically approved setup with a deep (30 cm) focus was compared with fully unfocused and diverging beams. These transmit beam profiles were used to investigate the beamwidth and uniformity versus depth, as well as the relative penetration. Furthermore, the receive beam sampling can be seen relative to beam profile uniformity. No transmit or receive apodization was used. For all sequences the surface, temperature was the limiting factor and the same aperture, and thus also transmit voltage, was used for all cases.

TABLE II
STRAIGHT TUBE SIMULATION PARAMETERS

Transducer type	Phased array
Aperture size [cm]	1.44
Azimuth focus [cm]	-9, 30
Elevation focus [cm]	5
Pulse center frequency [MHz]	3.3
No. of tx beams	1, 7
PRF [kHz]	3
Packet size	16
No. of frames	20
SNR	30
Straight tube radius [cm]	0.75
Straight tube tilt [°]	0
Straight tube depths [cm]	4.5, 7, 9.5
Straight tube V_{\max} [m/s]	1
Tracking kernel size [mm ²]	1x1

D. Clutter Filtering

The IQ-packet data from the *in vivo* color flow acquisitions were high-pass filtered to attenuate the strong clutter signal before blood velocity estimation. For ST velocity estimation, time-invariant clutter filters are preferred to avoid speckle image decorrelation due to the filter itself. However, for increasing packet sizes (> 16), the polynomial regression filters may also be used as the decorrelation becomes negligible [14]. In this paper, a fourth-order finite-impulse-response filter with -3 -dB cutoff velocity of $v_{co} = 1/3 \cdot V_{\text{Nyquist}}$ was used for the packet sizes of 8–16. For the packet size of 22, a fifth-order polynomial regression filter could be utilized (-3 -dB cutoff velocity of $v_{co} = 0.22 \cdot V_{\text{Nyquist}}$).

E. Blood Speckle Tracking

In blood ST, the correlation between speckle and blood movement is utilized to obtain an angle-independent velocity estimate of the blood velocity [5]. Pattern matching techniques on the radio frequency (RF) or envelope data are used to find the speckle displacement from frame to frame, where normalized cross correlation (NXC) is commonly used as a reference. There are, however, alternative speed enhancing alternatives, such as sum-of-squared-differences (SSD) and sum-of-absolute-differences giving similar results [5], [14]. Spatial interpolation before tracking may be needed to obtain the desired velocity resolution, depending on the original sampling grid. Tracking on RF data generally has a better accuracy in the axial direction than envelope tracking, as the phase information is taken into account, and however, the high-sampling rate needed for the RF data quickly increases the amount of data, which must be processed.

In our pursue for a real-time implementation, a GPU-optimized ST algorithm was developed. IQ data from the color flow acquisition in our duplex setup were first linearly interpolated laterally using a constant variance output grid [15]. Hardware accelerated linear interpolation on

the GPU was used to further increase our velocity resolution without increasing the memory load. SSD was used as the pattern matching method on the envelope data between the subsequent frames in the Doppler packet. The resulting SSD matrices were averaged over the Doppler packet and the minimum in the averaged SSD matrix determined the initial blood speckle displacement. Parabolic subsample fitting on the each estimates' SSD matrix gave the final nondiscrete velocity estimate. The GPU implementation is running close to real-time on commodity hardware.

F. Forward–Backward Tracking

As reported in the literature [7], [16], artifacts can occur using ST in the transition between signals with different characteristics, i.e., velocity gradients, blood-to-noise, blood-to-clutter. The artifacts are observed as bias either toward or away from these regions. To overcome this, a forward–backward tracking (FBT) approach is introduced. Where forward tracking (FT) finds the best match for a spatial region from one frame to the next in time and backward tracking (BT) finds the best match from the second frame to the previous, the FBT is the average of the FT and the BT estimates. The concept is that the FT and BT estimates can both contain a bias, but in the opposite directions, which cancels out when averaged. The cost of the method is the processing time, which is almost doubled per tracking point.

A general expression for the SSD at the given coordinates u, v , can be written as follows x :

$$\text{SSD}(u, v, n, \Delta_{\text{lag}}) = \sum_{x,y} (IQ_{\text{env}}(x, y, n) - IQ_{\text{env}}(x + u, y + v, n + \Delta_{\text{lag}}))^2 \quad (1)$$

where IQ_{env} is the envelope of an IQ-data frame, with a packet acquisition represented in the last dimension. The sum over x and y represents the spatial region of a search kernel. Furthermore, the FT and BT methods are given by

$$\text{SSD}_{\text{FT}}(u, v) = \frac{1}{N-1} \sum_{i=0}^{N-2} \text{SSD}(u, v, i, 1) \quad (2)$$

$$\text{SSD}_{\text{BT}}(u, v) = \frac{1}{N-1} \sum_{i=0}^{N-2} \text{SSD}(u, v, i+1, -1) \quad (3)$$

where the conventional FT method uses the positive lag and the BT changes the reference frame with the search frame. The SSD matrices are averaged over the packet size, N .

The position of the minimum of the SSD functions relative to the center is used as the expected discrete shift, as described in 4 where * denotes either FT or BT

$$[\Delta_{*x}, \Delta_{*z}] = \text{argmin}_{u,v} (\text{SSD}_*) \quad (4)$$

To further get the subpixel shift, parabolic minimum fitting of the SSD function is used for each dimension separately. Equation 5 describes the procedure where the SSD index is

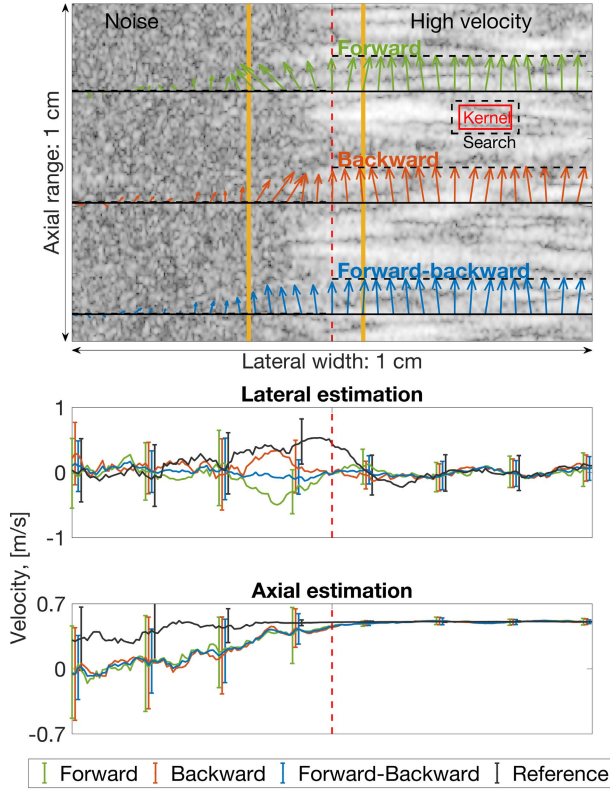


Fig. 1. Tracking performance under a simulated noise-to-flow condition. The bottom panels show the estimated velocities mean and standard deviation in the lateral direction for the lateral and axial components, respectively. A bias toward noise is observed outside the flow region for the FT estimates.

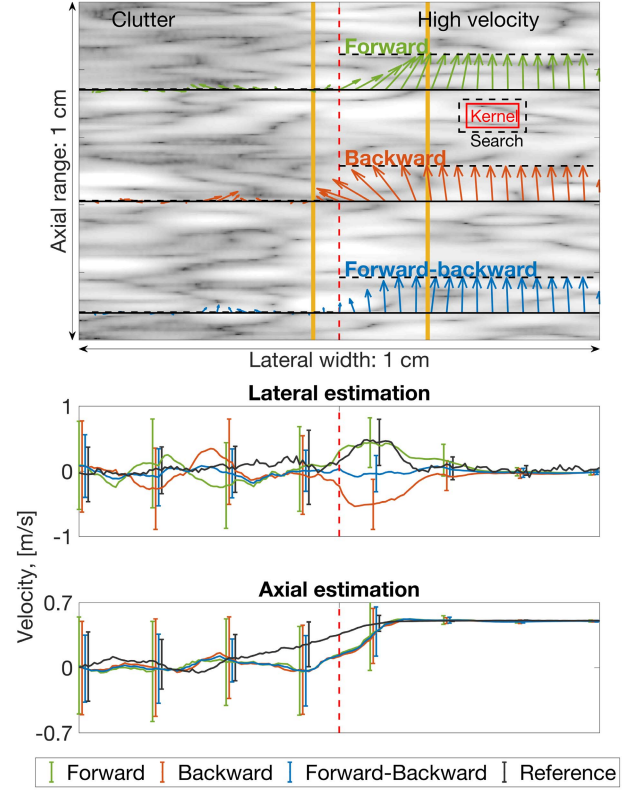


Fig. 2. Tracking performance under a simulated clutter-to-flow condition. The bottom panels show the estimated velocities mean and standard deviation in the lateral direction for the lateral and axial components, respectively. A bias toward flow is observed inside the flow region for the FT estimates.

relative to the found minimum from 4 in the direction of the subpixel shift to calculate

$$\delta_* = \frac{SSD_*(-1) - SSD_*(+1)}{2(SSD_*(-1) - 2SSD_*(0) + SSD_*(+1))}. \quad (5)$$

The final velocity estimates for FT and BT are given by 8, and for the FBT method by 8. Note the negative sign in 8 for BT

$$\vec{V}_{FT} = \frac{[\Delta_{FTx} + \delta_{FTx}, \Delta_{FTz} + \delta_{FTz}]}{PRF} \quad (6)$$

$$\vec{V}_{BT} = -\frac{[\Delta_{BTx} + \delta_{BTx}, \Delta_{BTz} + \delta_{BTz}]}{PRF} \quad (7)$$

$$\vec{V}_{FBT} = (\vec{V}_{FT} + \vec{V}_{BT})/2. \quad (8)$$

The raw tracking estimates can have high variance, in particular the lateral velocity component. Spatial and temporal smoothing is utilized to lower variance for better impression of the flow fields. See details in Table I.

III. RESULTS

A. Forward-Backward Tracking

Investigations of the FBT method were done for two simplified simulation setups. The simulated data were generated using the simulation tool FUSK (Fast Ultrasound Simulation in K-space) [17], which assumes a spatially invariant point-spread-function (PSF), but simulates realistic IQ data very rapidly. The results are shown in Figs. 1 and 2. Fig. 1 shows

TABLE III

FUSK SIMULATIONS, FORWARD-BACKWARD TRACKING

Flow RMSE (x/z), [cm/s]	Noise-to-flow	Clutter-to-flow
Forward tracking	27.4/4.39	33.1/19.0
Backward tracking	26.1/4.77	34.9/18.6
Forw.-back. tracking	22.6/3.82	17.6/17.6
Reference tracking	31.2/0.95	33.2/6.53

the simulated moving blood signal at 50 cm/s with a weak, close to stationary, and neighboring signal at 0.1 cm/s. The slowly moving signal is dominated by noise after clutter filtering. Fig. 2 shows the same signals, however, with a lower SNR and a stronger stationary signal resulting in a stationary region dominated by decorrelation due to clutter filtration and the conflicting signals. The specifics are shown in Table III and Fig. 3. An observation from both the results is the transitional region between the signals, due to the PSF and the tracking kernel, resulting in a gradual change in the tracking estimates from one region to the other. In both cases, we observe an opposite lateral bias in the separated forward and backward estimates and a magnitude bias on the axial component. The extent of the bias depends on the scenario, but in both cases, the FBT approach significantly reduces the error. In the noise and flow signal scenario (see Fig. 1), the bias is first observed outside the signal border, where we see a gradual bias toward the noise. We still see an improvement of the estimates inside

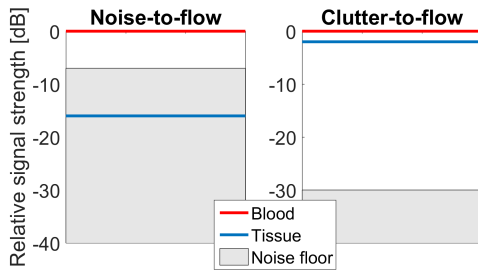


Fig. 3. Relative signal strengths after clutter filtering for the two scenarios.

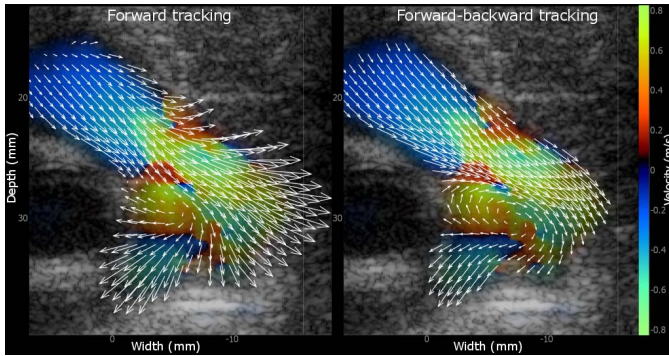


Fig. 4. Comparison of FT and FBT in an *in vivo* example of flow in the pulmonary artery of a newborn (patient 1). The effect of biased velocity estimates is greatly reduced in the image to the right.

the flow region with a decrease of 17% and 13% in root mean square (rms) error, compared with FT, for the lateral and axial components, respectively. For the clutter and flow signal scenario, the bias also occurs inside the flow region. In this case, the FBT approach reduced the rms error with 47% and 6.6% for the two components, respectively. For comparison, the tracking was also done using RF data and NXC as a reference. The lateral bias was comparable between RF NXC and our method in the clutter-to-flow scenario in Fig. 2, but in the poor SNR scenario in Fig. 1, RF tracking can be observed to perform worse for the lateral velocity estimation.

A comparison of the difference between FT and FBT *in vivo* is shown in Fig. 4. While the conventional FT method is occluded by a bias toward the surrounding wall, the FBT is not. The vortex appearing in the pulmonary artery of patient 1 with a PV stenosis is in this case only visible when using FBT.

B. Beam Profile Comparison

Measured lateral beam profiles for the 6S phased array probe for deeply focused (30 cm), unfocused, and defocused (focus located 9 cm behind the transducer) transmit beams are shown to the right in Fig. 5 for five depths. The five depths are indicated with horizontal lines to the left in Fig. 5, and the 16 receive lines are shown as dashed lines. The deeply focused and unfocused beams are similar close to the transducer, but in depth, the beam focused at 30 cm is narrower. At 9 cm, the difference between the center and edge of the beam is about 9 dB for the deeply focused compare to 6 dB for the unfocused beam. The slightly diverging beam is still approximately plane at this depth, but the beam intensity lies about 3–6 dB below the two others.

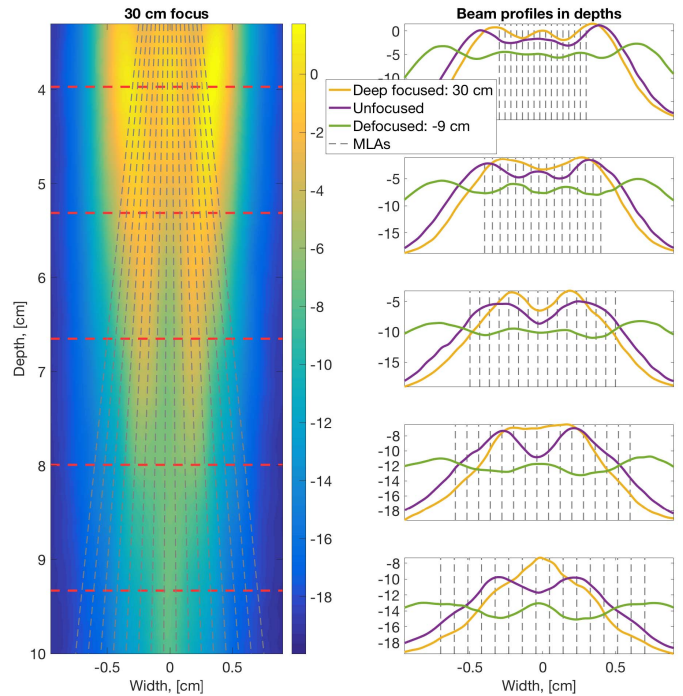


Fig. 5. Measured beam profiles for the 6S phased array probe for deeply focused (30 cm), unfocused, and defocused (focus located 9 cm behind transducer) transmit beams. To the left is an image of the transmit beam focused at 30 cm. The five depths for the lateral beam profiles shown to the right are indicated with horizontal lines. The receive lines are shown as dashed lines.

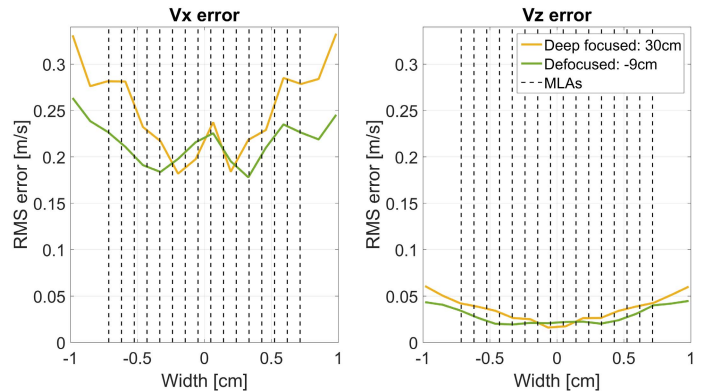


Fig. 6. Mean rms error over 20 simulated straight tubes at 9.5-cm depth. Left: rms error for the estimated V_x -component. Right: rms error for the estimated V_z -component. Vertical dashed lines: extent of the 16 receive lines (MLAs).

As can be observed, the 16 receive lines span a substantially nonuniform lateral beam profile for deeper regions for the deeply focused beam. A lower accuracy is expected for these regions, and only the inner receive lines should ideally be used in this case. Moving to (slightly) diverging beams, this is not an issue, but the uniformity comes at the cost of 3–6-dB loss in SNR. If supported by the system, a higher number of parallel receive lines could then also be used.

C. Straight Tube Simulations

First, the accuracy of the tracking estimates over the MLA group was investigated. The straight tube was placed at 9.5-cm

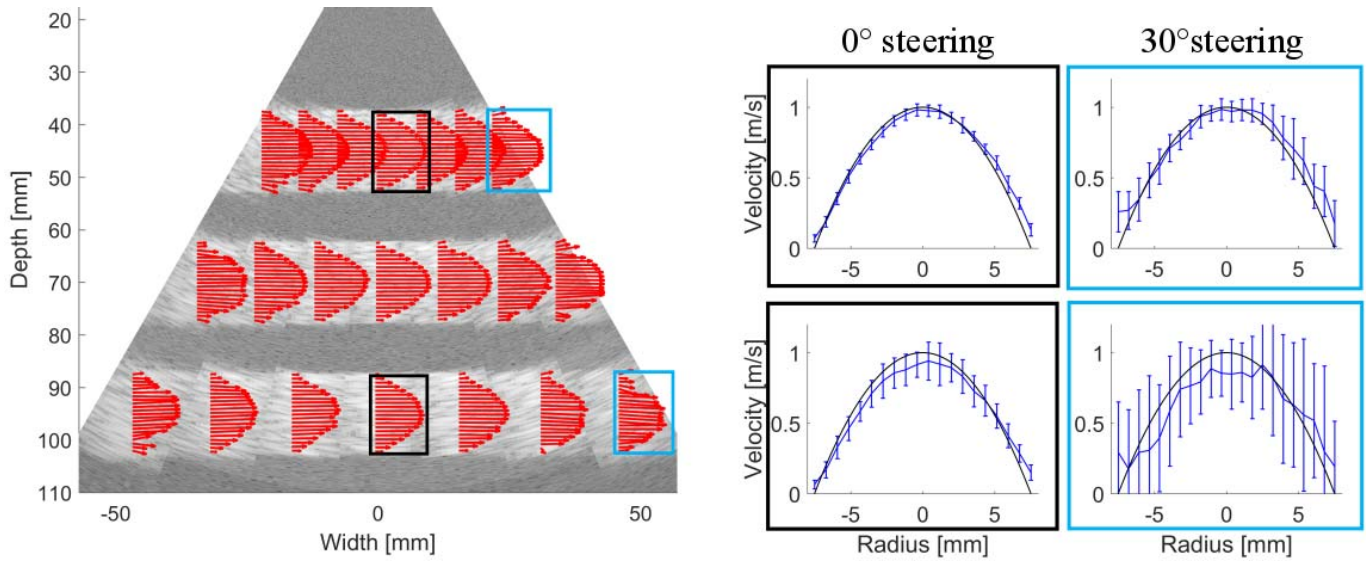


Fig. 7. Left: ST velocity profiles from straight tube simulations for three different depths. Right: four profiles (middle and far right for depth 4.5 and 9.5 cm) shown with standard deviation and the reference velocity (black line).

TABLE IV
ESTIMATED VELOCITY AT TUBE CENTER LINE FOR DIFFERENT DEPTHS AND STEERING ANGLES

Steering angle [°]	-30	-20	-10	0	10	20	30
Expected $ V $ [m/s]	1.0	1.0	1.0	1.0	1.0	1.0	1.0
$ V @45\text{mm}$ [m/s]	0.98 ± 0.06	0.97 ± 0.06	0.98 ± 0.06	0.98 ± 0.04	0.99 ± 0.04	0.97 ± 0.06	0.98 ± 0.07
$ V @70\text{mm}$ [m/s]	0.96 ± 0.12	1.01 ± 0.09	1.04 ± 0.09	1.05 ± 0.06	1.03 ± 0.10	1.02 ± 0.10	0.94 ± 0.13
$ V @95\text{mm}$ [m/s]	0.91 ± 0.19	0.90 ± 0.19	0.92 ± 0.14	0.93 ± 0.11	0.96 ± 0.12	0.88 ± 0.17	0.85 ± 0.21

depth and two acquisition schemes were simulated; a single deeply focused and a single slightly diverging transmit beams with a packet size of 16 for 20 frames. The rms error was calculated for both velocity components over the radius of the tube and averaged over the 20 simulated frames and the results are shown in Fig. 6. As expected from the beam profiles at depth 9.5 cm in Fig. 5, the mean rms error over the 20 Doppler frames for the deeply focused beam increased when moving outward from the center of the beam, especially for the V_x component. The mean rms error for the diverging beam did not increase as much over the MLA group. For the V_x -component, both the deeply focused and the diverging beam got a small rms error increase at the beam center.

Second, the accuracy of the tracking estimates when considering imaging depth and steering angle was investigated. Simulated straight tubes were placed at three depths (4.5, 7, and 9.5 cm) and seven deeply focused transmit beams were used to cover an opening angle of 60°. In Fig. 7 (left), the estimated velocity profiles for the three tubes are shown. The eight middle beams for each MLA group were averaged before the mean of the 20 simulated Doppler frames results in the final velocity profile. The middle transmit beam gave good results for all three depths, but as the beam was steered out, the velocity profile was clearly degraded in depth. To investigate more closely, four of the velocity profiles (from the middle and far right of depth 4.5 and 9.5 cm) are shown in Fig. 7 (right). The black lines indicate the

reference velocity and the estimated mean velocity profiles are shown with the standard deviation for the 20 simulated Doppler frames. The standard deviation increases with depth and steering angle. For the depth of 9.5 cm, the highest steering angle (30°) results in the high standard deviations of 20–50 cm/s and an underestimation of the highest velocities.

Table IV shows the estimated velocity at the tube center for the three depths and all seven steering angles. The reference velocity for all estimates are 1 m/s. For the depth of 4.5 cm, the maximum velocity is slightly underestimated and with a standard deviation for all steering angles < 7 cm/s. At 7 cm, the highest steering angle ($\pm 30^\circ$) deviates from the rest (which are slightly overestimated) with an underestimation of 4–6 cm/s and a standard deviation of 12–13 cm/s. For the deepest tube, a steering angle of 20° and above gives the underestimations of 9–15 cm/s and the standard deviations of about 20 cm/s.

D. Validation of Velocity Estimates

In Fig. 8, the ST velocity estimates in a small ROI are validated toward a conventional pulsed-wave (PW) Doppler recording from a corresponding ROI. The ST velocity estimates are averaged in the ROI (black square in the image in the left panel) and projected on to the PW acquisition beam axis. The resulting ST velocity trace is plotted on top of the PW Doppler spectrum in the right panel. The velocities in the

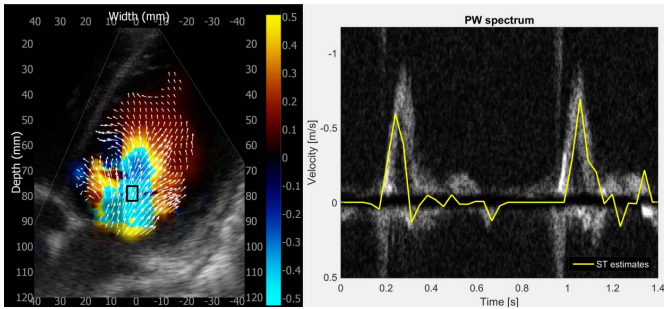


Fig. 8. Validation of ST estimates. Left: vector flow map overlaid color flow image of the left ventricle of patient 2 (DCM). Right: PW Doppler spectrum acquired from a separate recording. Yellow line: ST velocity trace from a corresponding ROI (black square in the left image). The ST velocities have been projected on to the PW acquisition beam for comparison.

ROI exceed the Nyquist velocity (0.5 m/s for the color flow acquisition) for the highest velocities, but, as can be observed, the ST velocity estimates still have a good correspondence with the PW Doppler spectrum. A small difference in heart rate is observed between the recordings.

E. In Vivo Results

In Fig. 9, patient 1, a newborn with a pulmonary stenosis, is imaged with both the 9L linear array and the 6S phased array probe. The images display the right ventricular outflow tract, the PV, and the main pulmonary artery branching into the left and right pulmonary artery. The 9L probe clearly provides the images of higher resolution compared with the 6S probe, by inspecting the B-mode speckle. The flow field characteristics are, however, similar, displaying the vortex forming in the dilated pulmonary artery distal to the valve.

Fig. 10 shows the 9L and 6S images for patient 2, an 11 years old with DCM. Both images are from the parasternal long-axis view, where the left atrium, the left ventricle and the left ventricular outflow tract are usually seen. However, a much smaller field-of-view is obtained with the linear array to the left than with the phased array to the right. In this case, it was not possible to image the whole ROI due to the narrow image view with the linear array. To the right, we can see two vortices forming behind the mitral valve leaflets as the ventricle is filled.

IV. DISCUSSION

Phased array probes have been tested for the purpose of achieving detailed cardiac flow images of pediatric patients with 2-D blood ST. We have previously reported that linear arrays can be used to image neonatal hearts as we can image straight through the ribs [6], and however, the standard pediatric probes are phased array probes and the aim here was to further develop our methods for these probes, which are more appropriate when imaging older children.

To improve the ST velocity estimation, a FBT approach was introduced, which efficiently reduced bias occurring toward the edges of the flow domain, as shown in Fig. 4. In the simple simulations of pure axial motion in Figs. 1 and 2, it was observed two different bias effects depending on the interfering signals. The direction of the lateral bias was related

to the signal sources in the tracking kernel. If the tracking kernel partly contained noise, the lateral bias was toward the noise region for FT. If the tracking kernel contained both decorrelated and correlated signals, the lateral bias pointed toward the correlated (high velocity) region for FT. In both cases, BT gave a bias in the opposite direction, which resulted in the forward-backward averaging removing the bias. For comparison, NXC on RF data was performed as a reference method toward our method with SSD envelope tracking. In the lateral direction, RF and envelope tracking are in general comparable, and the lateral bias was present in both simulations. RF tracking was observed to be more susceptible to noise resulting in a lateral bias covering a larger region in the noise-to-flow scenario in Fig. 1. Nevertheless, RF tracking has a higher accuracy and lower variance in the axial direction [14].

The drawback of FBT was the increased tracking time (tracking both in the forward and backward directions), but with the GPU-optimized tracking code, the tracking times were still close to real time (some seconds per cardiac cycle for a high-end GPU), providing bedside applicability. As ST results are dependent on spatiotemporal averaging, the FBT approach is especially useful when the blood domain is small. With larger domains, as in the heart lumen, this effect can be defeated by trimming the tracking domain before smoothing. However, this is not necessarily straightforward, and the bias may still be included in the averaging window and occlude important flow features, as shown in Fig. 4.

In our clinical approved real-time imaging setup, we were limited to a 30-cm focus depth and 16 parallel receive lines. Several transmissions were needed to cover the desired ROI which, together with the B-mode acquisition, decreases the total frame rate. Due to diffraction effects, the width of the plane wavefront are reduced in depth as shown in Fig. 5, and thus, several plane waves would be needed to cover the ROI regardless of the limited number of receive lines. When the image depths exceed 8 cm, the amplitude of both the unfocused and the deeply focused beam falls off when getting closer to the diffraction focus. The loss in SNR on the flanks results in poorer tracking performance on the edges of the MLA groups in depth, as shown in Fig. 6. The peak observed at the beam center for the V_x -component in Fig. 6 can arise from the higher variance in the lateral tracking component compared with the axial tracking component, and in the beam center only the lateral tracking component contributes to the V_x -component.

For diverging wave transmissions, a larger ROI could be covered with only one or a few transmissions. However, for phased-arrays, the lower pressure versus depth as shown in Fig. 5 would result in a reduced SNR and penetration. It is, unfortunately, not straightforward to utilize coherent compounding to retain this SNR due to the high-Doppler PRF needed in this clinical context. However, the increased frame rate could be utilized to increase packet size and thus improve clutter filtering and blood flow detection.

The spatial resolution is poorer with the general pediatric phased array compared with a linear array due to the smaller aperture and lower frequency range. The phased array operation also results in a highly depth-dependent lateral resolution,

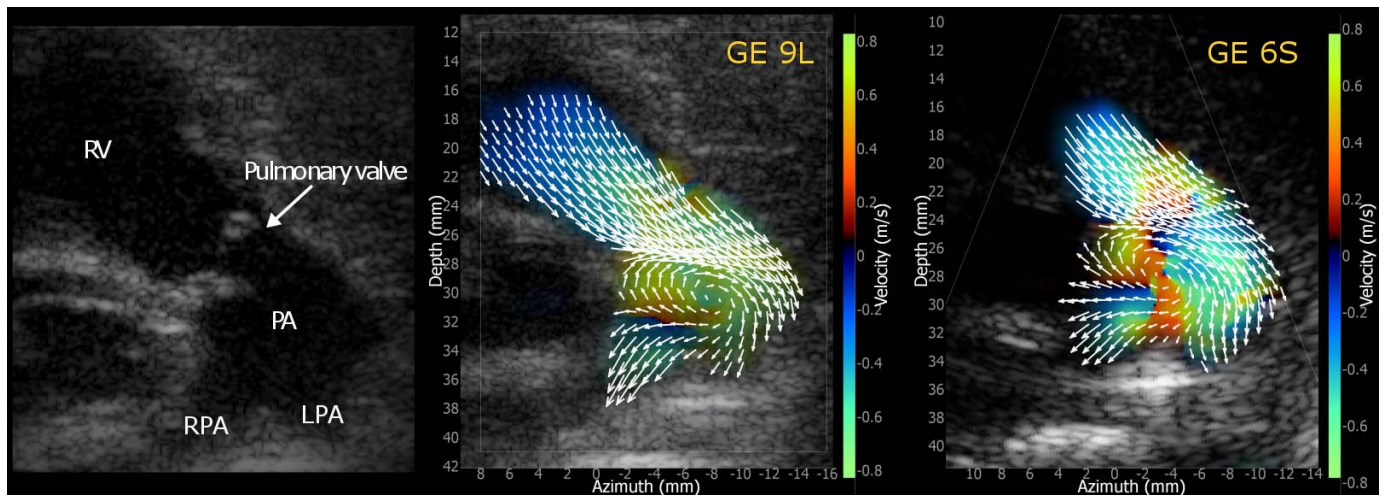




Fig. 9. Ten-day-old newborn with a PV stenosis imaged with both the GE 9L linear array  and the GE 6S phased array . RV = right ventricle, PA = pulmonary artery, and LPA/RPA = left/right pulmonary artery branch. The ST velocity estimates are shown as arrows overlaid the color flow image. The large vortex forming in the main PA is seen in both recordings.

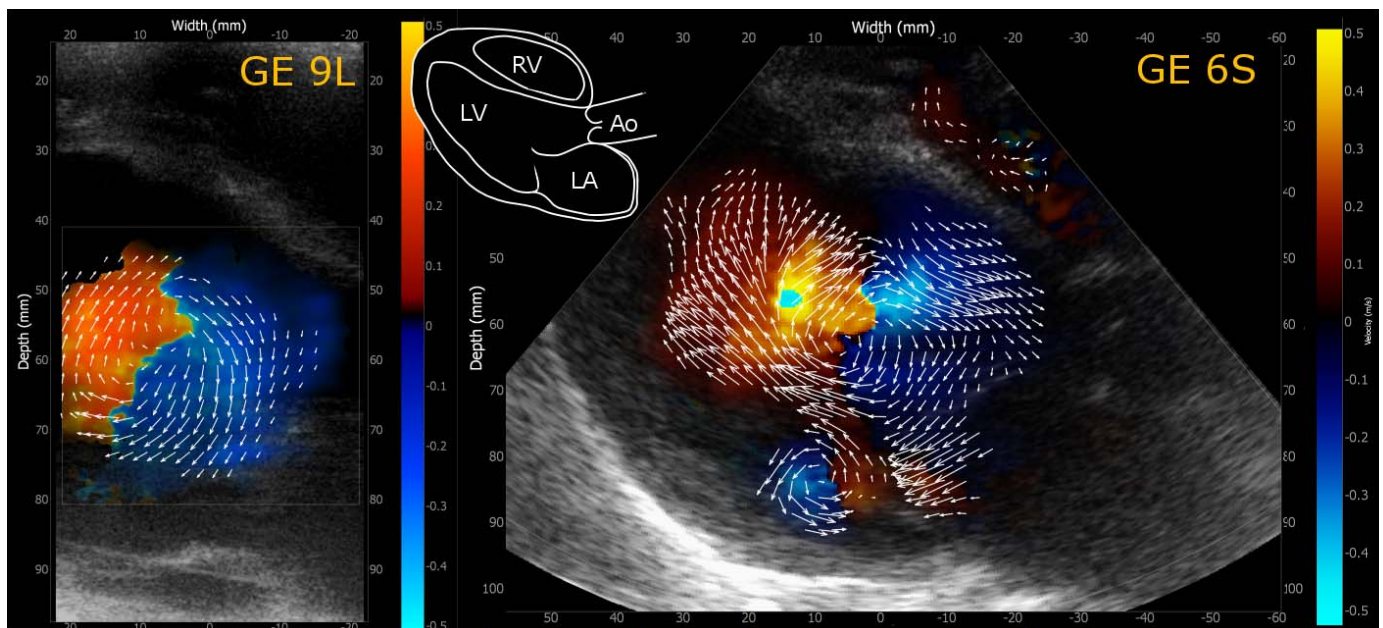




Fig. 10. Eleven-year-old child with DCM imaged with both the GE 9L linear array  and the GE 6S phased array . LA = left atrium, LV = left ventricle, RV = right ventricle, and Ao = aorta. The field of view obtained with the linear array is limited. In the phased-array image, two vortices are forming behind the mitral valve leaflets.

which degrades the lateral tracking quality increasingly for larger depths and steering angles, as shown in Fig. 7. It could, in this setting, be beneficial to use a depth-dependent tracking kernel, which was not used in this paper.

Despite the current drawbacks, our experience and preliminary validation toward spectral Doppler in Fig. 8 and comparisons with linear array imaging in Figs. 9 and 10 show promising results. In the patients we have imaged (the image depths of <10 cm), vortex formation in the cardiac chambers could be mapped, in addition to a qualitative impression of the primary and secondary blood flow patterns.

V. CONCLUSION

Pediatric phased array probes utilizing broad (deeply focused) pulses and blood ST were used to image complex

flow patterns in two pediatric patients with a congenital heart disease. FBT proved important to alleviate a tracking bias occurring at the edges of the flow domain. While promising results were demonstrated for image depths <10 cm, limitations in penetration are expected compared with conventional CFI, and a larger feasibility study is needed to map the true clinical potential of the approach.

REFERENCES

- [1] D. van der Linde *et al.*, “Birth prevalence of congenital heart disease worldwide: A systematic review and meta-analysis,” *J. Amer. College Cardiol.*, vol. 58, no. 21, pp. 2241–2247, Nov. 2011.
- [2] O. J. Benavidez, K. Gauvreau, K. J. Jenkins, and T. Geva, “Diagnostic errors in pediatric echocardiography: Development of taxonomy and identification of risk factors,” *Circulation*, vol. 117, no. 23, pp. 2995–3001, Jun. 2008.

- [3] M. S. Chew and J. Poelaert, "Accuracy and repeatability of pediatric cardiac output measurement using Doppler: 20-year review of the literature," *Intensive Care Med.*, vol. 29, no. 11, pp. 1889–1894, 2003.
- [4] G. Pedrizzetti, G. La Canna, O. Alfieri, and G. Tonti, "The vortex—An early predictor of cardiovascular outcome?" *Nature Rev. Cardiol.*, vol. 11, no. 9, pp. 545–553, 2014.
- [5] L. N. Bohs, B. J. Geiman, M. E. Anderson, S. C. Gebhart, and G. E. Trahey, "Speckle tracking for multi-dimensional flow estimation," *Ultrasonics*, vol. 38, nos. 1–8, pp. 369–375, Mar. 2000.
- [6] S. Fadnes, S. A. Nyernes, H. Torp, and L. Lovstakken, "Shunt flow evaluation in congenital heart disease based on two-dimensional speckle tracking," *Ultrasound Med. Biol.*, vol. 40, no. 10, pp. 2379–2391, 2014.
- [7] J. Van Cauwenberge *et al.*, "Assessing the performance of ultrafast vector flow imaging in the neonatal heart via multiphysics modeling and *in vitro* experiments," *IEEE Trans. Ultrason., Ferroelect., Freq. Control*, vol. 63, no. 11, pp. 1772–1785, Nov. 2016.
- [8] H. Takahashi, H. Hasegawa, and H. Kanai, "Echo speckle imaging of blood particles with high-frame-rate echocardiography," *Jpn. J. Appl. Phys.*, vol. 53, no. 7S, pp. 07KF08-1–07KF08-7, 2014.
- [9] G.-R. Hong *et al.*, "Characterization and quantification of vortex flow in the human left ventricle by contrast echocardiography using vector particle image velocimetry," *JACC, Cardiovascular Imag.*, vol. 1, no. 6, pp. 705–717, Nov. 2008.
- [10] H. Gao, N. Bijnens, D. Coisne, M. Lugiez, M. Rutten, and J. D'hooge, "2-D left ventricular flow estimation by combining speckle tracking with Navier–Stokes-based regularization: An *in silico*, *in vitro* and *in vivo* study," *Ultrasound Med. Biol.*, vol. 41, no. 1, pp. 99–113, Jan. 2015.
- [11] S. Fadnes, S. A. Nyernes, M. Wigen, E. Tegnander, and L. Lovstakken, "Detailed flow visualization in fetal and neonatal hearts using 2-D speckle tracking," in *Proc. IEEE Int. Ultrason. Symp. (IUS)*, Sep. 2016, pp. 8–11.
- [12] J. A. Jensen and N. B. Svendsen, "Calculation of pressure fields from arbitrarily shaped, apodized, and excited ultrasound transducers," *IEEE Trans. Ultrason., Ferroelect., Freq. Control*, vol. 39, no. 2, pp. 262–267, Mar. 1992.
- [13] J. A. Jensen, "Field: A program for simulating ultrasound systems," presented at the 10th Nordic-Baltic Conf. Biomed. Imag. Published Med. Biol. Eng. Comput., vol. 34, 1996, pp. 351–353.
- [14] S. Fadnes, S. Bjærum, H. Torp, and L. Lovstakken, "Clutter filtering influence on blood velocity estimation using speckle tracking," *IEEE Trans. Ultrason., Ferroelect., Freq. Control*, vol. 62, no. 12, pp. 2079–2091, Dec. 2015.
- [15] O. Salvado and D. L. Wilson, "Removal of local and biased global maxima in intensity-based registration," *Med. Image Anal.*, vol. 11, no. 2, pp. 183–196, 2007.
- [16] S. Fadnes, S. A. Nyernes, A. Swillens, H. Torp, and L. Lovstakken, "Shunt quantification in congenital heart disease based on two-dimensional speckle tracking," in *Proc. IEEE Int. Ultrason. Symp. (IUS)*, Oct. 2012, pp. 1877–1880.
- [17] T. Hergum, S. Langeland, E. W. Remme, and H. Torp, "Fast ultrasound imaging simulation in K-space," *IEEE Trans. Ultrason., Ferroelect., Freq. Control*, vol. 56, no. 6, pp. 1159–1167, Jun. 2009.



Solveig Fadnes was born in Ålesund, Norway, in 1986. She received the M.Sc. degree in applied physics and the Ph.D. degree in medical technology from the Norwegian University of Science and Technology (NTNU), Trondheim, Norway, in 2010 and 2013, respectively.

She is currently a Post-Doctoral Fellow with the Department of Circulation and Medical Imaging, NTNU. Her current research interests include signal processing and blood flow imaging in diagnostic ultrasound, with a focus on intracardiac blood flow quantification.



Morten Smedsrud Wigen was born in Oslo, Norway, in 1988. He received the M.Sc. degree in electronics from the Norwegian University of Science and Technology, Trondheim, Norway, in 2014, where he is currently pursuing the Ph.D. degree in medical technology with the Department of Circulation and Medical Imaging, with a focus on 3-D intracardiac vector flow imaging.



Siri Ann Nyernes was born in Lesja, Norway, in 1969. She received the M.D. degree in medicine and the Ph.D. degree in medical technology from the Norwegian University of Science and Technology (NTNU), Trondheim, Norway, in 1995 and 2014, respectively.

She has been a Board Certified Specialist in pediatrics since 2005. She currently combines clinical work as a Consultant in pediatric cardiology with the Department of Pediatrics, St. Olav's University Hospital, Trondheim, with clinical research in cooperation with the Ultrasound Research Group, NTNU. Since 2012, she has been a Board Member of the Norwegian Congenital Heart Disease Group. Her main research interest is pediatric echocardiography.



Lasse Lovstakken received the M.Sc. degree in engineering cybernetics and the Ph.D. degree in medical ultrasound imaging technology from the Norwegian University of Science and Technology (NTNU), Trondheim, Norway.

He is currently a Professor with the Department of Circulation and Medical Imaging, NTNU. His main clinical focus has been cardiovascular imaging with emphasis on methods for improved estimation of blood velocities in the heart and vessels. His current research interests include signal and image processing applied in medical ultrasound imaging for improved image formation, and the detection and estimation of moving tissue and blood flow.